Floquet engineering the quantum Rabi model in the ultrastrong coupling regime

– SUPPLEMENTARY INFORMATION –

Kamran Akbari,[1,*] Franco Nori,[2,3,4] and Stephen Hughes[1]

[1] *Department of Physics, Engineering Physics and Astronomy, Queen's University, Kingston ON K7L 3N6, Canada*

[2] *Theoretical Quantum Physics Laboratory, Cluster for Pioneering Research, RIKEN, Wakoshi, Saitama 351-0198, Japan*

[3] *Quantum Computing Center, RiKEN, Wakoshi, Saitama, 351-0198, Japan*

[4] *Physics Department, The University of Michigan, Ann Arbor, Michigan 48109-1040, USA*

(Dated: February 6, 2025)

In this Supplementary Information document, we present further details of the system Hamiltonian we use for the time-dependent quantum Rabi model, as well as the general Floquet theory, and include additional results and discussions, further numerical simulations, as well as different modulation profiles for the time-dependent oscillations (specifically, different from the purely sinusoidal case shown in the main text).

CONTENTS

* kamran.akbari@queensu.ca

S1. SYSTEM HAMILTONIAN AND GAUGE INVARIANCE FOR THE MATTER-TRUNCATED QUANTUM RABI MODEL

We consider a typical cavity-quantum electrodynamic (QED) system made up of a single atom coupled to a single-mode optical cavity, described by the quantum Rabi model (QRM). In the dipole gauge (specifically, the dipole approximation in the multipolar gauge), the QRM describes the TLS-cavity system via the Hamiltonian [1, 2] (in units of $\hbar = 1$):

$$\mathcal{H}_{\rm QR}^{\rm D} = \omega_{\rm c} a^\dagger a + \frac{\omega_a}{2}\sigma_z + {\rm i}g(a^\dagger - a)\sigma_x, \tag{S1}$$

up to a constant ($\mathbf{1}\omega_c\eta^2$), where ω_c is the cavity transition frequency, a ($a^\dagger$) is the cavity photon annihilation (creation) operator, ω_a is the TLS transition frequency, $\sigma_z = \sigma^+\sigma^- - \sigma^-\sigma^+$ and $\sigma_x = \sigma^+ + \sigma^-$, with $\sigma^+ = |e\rangle\langle g|$ ($\sigma^- = |g\rangle\langle e|$) the atomic raising (lowering) operator; also, g is the atom-cavity coupling in the dipole gauge ($g \propto \sqrt{\omega_c}$), and $\eta = g/\omega_c$ is the normalized coupling parameter.

When the system is subjected to matter truncation, $\mathcal{H}_{\rm QR}^{\rm D}$ produces the correct eigenenergies [3], and following the steps outlined in Ref. [2] for the time-independent Hamiltonian, by applying an appropriate unitary gauge transformation (namely, the Power–Zienau–Woolley transformation modified in the truncated matter space) to the dipole gauge-independent QRM model, the correct *gauge-fixed* Coulomb QRM Hamiltonian is [2]

$$\mathcal{H}_{\rm QR}^{\rm C} = \omega_{\rm c} a^\dagger a + \frac{\omega_a}{2}\left(\sigma_z \cos[2(a+a^\dagger)\eta] + \sigma_y \sin[2(a+a^\dagger)\eta]\right), \tag{S2}$$

which produces identical eigenenergies to $\mathcal{H}_{\rm QR}^{\rm D}$. This modification to the Hamiltonian arises due to the canonical transformation of the field coordinates that does not alter the Hamiltonian with the time-independent constraints [4]. The nonperturbative nature of the quantum light-matter interaction in the USC regime forces the gauge correction due to the emergence of a nonlocal potential of the truncated matter (the TLS) part originating in the dipole gauge, and then gauge-transformed to the Coulomb gauge. This gauge-correction appears in a transcendental trigonometric form in the Coulomb gauge, implying its nonperturbative nature [2].

Our goal is to incorporate the time variation to the system Hamiltonian nonperturbatively via applying Floquet theory in the USC regime of cavity QED or the QRM, where the defining features are caused by Hamiltonian interactions of the form $g(a+a^\dagger)(\sigma^+ + \sigma^-)$ [or for coupled bosons $g(a+a^\dagger)(b+b^\dagger)$], which is required when $g/\omega_0 > 0.1$ with ω_0 being a typical transition energy scale in the system (usual definition of the USC regime). Keeping the counter rotating-wave terms (e.g., $a\sigma^-$, $a^\dagger\sigma^+$) in the system-level interaction Hamiltonians is the crux of USC (these cannot be dropped). To ensure gauge invariance for a truncated matter system, and also to include time-dependent interactions, it is preferable and easier to use the Coulomb gauge picture for the Hamiltonian [4, 5], which takes the form

$$\mathcal{H}_{\rm FQR}^{\rm C}(t) = \omega_c a^\dagger a + \frac{\omega_a}{2}\left\{\sigma_z \cos\left[2(a+a^\dagger)\eta(t)\right] + \sigma_y \sin\left[2(a+a^\dagger)\eta(t)\right]\right\}, \tag{S3}$$

which we refer to as a *Floquet-engineered quantum Rabi* (FQR) Hamiltonian as we will consider periodic time-modulations as discussed below. In the Coulomb gauge, the time-dependence of the cavity-matter coupling is simply included through the time-dependent coupling rate, which we define from $\eta(t) = \eta_0 + \eta_M(t)$, with the dynamical part having the peak value of η_M. Calligraphic notation is used to clarify that we model the truncated quantum system [2, 4, 6]. Without time-modulation, then $\eta_0 = g/\omega_c$ is the usual form for the truncated-matter QRM, $\mathcal{H}_{\rm QRM} = \mathcal{H}_{\rm FQR}(0)$.

It has been shown in Refs. [4, 5] that while the treatment of an arbitrary time-dependece in the multipolar gauge has severe complications, e.g., the quantization procedure must undergo with time-dependence constraint [4], it is easy to directly adapt the time-dependence in the Coulomb gauge. Hence, we obtain the FQR Hamiltonian as the form given in Eq. (S3). We next rewrite this Hamiltonian by representing the trigonometric functions via exponential functions, dropping the explicit "C" superscript, in a form that will make the FQR model Hamiltonian clearer:

$$\mathcal{H}_{\rm FQR}(t) = \omega_{\rm c} a^\dagger a + \frac{\omega_a}{2}\left\{\frac{\sigma_z - {\rm i}\sigma_y}{2}\,{\rm e}^{{\rm i}2(a+a^\dagger)\eta_0}\,{\rm e}^{{\rm i}2(a+a^\dagger)\eta_M(t)} + \frac{\sigma_z + {\rm i}\sigma_y}{2}\,{\rm e}^{-{\rm i}2(a+a^\dagger)\eta_0}\,{\rm e}^{-{\rm i}2(a+a^\dagger)\eta_M(t)}\right\}. \tag{S4}$$

It is also worth noting that if one naively uses the dipole-gauge Hamiltonian model to Floquet engineer the QRM, it follows that

$$\mathcal{H}_{\rm FQR}^{\rm D,naive}(t) = \omega_c a^\dagger a + (\omega_a/2)\sigma_z - {\rm i}g(t)\sigma_x(a^\dagger - a),$$

then letting $g(t) = g_0 + g_M \sin(\omega_M t)$, the model reads

$$\mathcal{H}_{\rm FQR}^{\rm D,naive}(t) = \mathcal{H}_{\rm QR}^{\rm D} - {\rm i}g_M \sin(\omega_M t)\sigma_x(a^\dagger - a).$$

This model is *gauge-dependent* and does *not* produce a renormalization of the QRM (it is simply *not* correct to use such a model with time-dependent interactions, as described in detail in [4]). The renormalization of the QRM in the *corrected* Coulomb gauge is a result of correct gauge-invariant model treated nonperturbatively and is *substantially different* from the usual DC/AC Stark shift. This time-modulated USC effect is even more striking as it causes an effective splitting of the eigenenergy lines, even if there is no initial splitting due to light-matter dressing (i.e., when $\eta_0 = 0$), and it enhances the creation of effective anticrossings in the Floquet picture for all values of η_0 (see Fig. 2 in the main text). Moreover, it may only occur in the Floquet engineering of a quantum system *not* simply Floquet driving, and it produced real photons with no input photons.

S2. FLOQUET THEORY AND FLOQUET-DRESSING THE QUANTUM RABI MODEL

Since we consider a time-periodic Hamiltonian, we can write a solution (quasienergy state) of the time-dependent Schrödinger equation (TDSE), $\mathrm{i}\partial_t|\psi(t)\rangle = \mathcal{H}_{\rm FQR}(t)|\psi(t)\rangle$, yielding a Floquet state, in the form of $|\psi_\alpha(t)\rangle = \mathrm{e}^{-\mathrm{i}\varepsilon_\alpha t}|\alpha(t)\rangle$, where ε_α the Floquet (time-independent) quasienergy [7], and $|\alpha(t)\rangle$ is a T-periodic, Floquet mode (analogous to Bloch modes in periodic lattices). Although these are also quantum states, we use the term "mode" to be consistent with the common literature on Floquet theory, where $|\psi_\alpha(t)\rangle$ are termed Floquet states, $|\alpha(t)\rangle$ are Floquet modes, and $|\alpha_l\rangle$, defined below, refer to the lth sideband of the Floquet state [8].

The Floquet Hamiltonian is then defined from $\mathcal{H}_{\rm F}(t) \equiv \mathcal{H}_{\rm FQR}(t) - \mathrm{i}\partial/\partial t$, associated with a set of quasienergies $\{\varepsilon_\alpha\}$. Therefore, $|\alpha(t)\rangle$ is an eigenket of the Floquet Hamiltonian $\mathcal{H}_{\rm F}(t)$, where

$$\mathcal{H}_{\rm F}(t)|\alpha(t)\rangle = \varepsilon_\alpha|\alpha(t)\rangle. \tag{S5}$$

Although time-dependent, the set of Floquet states, $\{|\psi_\alpha(t)\rangle\}$, form a complete basis for any value of t, and as such, the general solution to the TDSE can be expanded in terms of the Floquet states, i.e., $|\psi(t)\rangle = \sum_\alpha c_\alpha|\psi_\alpha(t)\rangle$, where $c_\alpha = \langle\alpha|\psi(0)\rangle$, with $|\alpha\rangle \equiv |\alpha(0)\rangle$, are time-independent complex coefficients. If the system is prepared in a single Floquet state, $|c_\alpha| = \delta_{\alpha\alpha_0}$, its time evolution will be periodic and (apart from the irrelevant overall phase factor, $\mathrm{e}^{-\mathrm{i}\varepsilon_{\alpha_0}t}$) can be described by the Floquet mode $|\alpha_0(t)\rangle$. If the system is prepared in a coherent superposition of several Floquet states, the time evolution will no longer be periodic in general and will instead be determined by two contributions [8]: (i) the contribution that stems from the periodic time dependence of the Floquet modes $|\alpha(t)\rangle$ (called the micromotion contribution), and (ii) the contribution which leads to deviations from a periodic evolution, originating from the relative dephasing of the factors $\mathrm{e}^{-\mathrm{i}\varepsilon_\alpha t}$. Thus, beyond the periodic micromotion, the time evolution of a Floquet system is governed by the quasienergies ε_α of the Floquet states in much the same way as the time evolution of an autonomous system (with time-independent Hamiltonian) is governed by the energies of the stationary states [9].

As the modes $|\alpha(t)\rangle$ are periodic, Eq. (S5) suggests that energies in Floquet systems are only conserved modulo ω_M, and it can be shown that the transition resonances of the system occur at differences between Floquet quasienergies [10]. The periodicity of the Floquet modes also suggests writing them as a Fourier series

$$|\alpha(t)\rangle = \sum_{l\in\mathbb{Z}} \mathrm{e}^{\mathrm{i}l\omega_M t}|\alpha_l\rangle, \tag{S6}$$

where $|\alpha_l\rangle$ are the Fourier coefficients, called Floquet sidebands, with the normalization condition $\sum_l\langle\alpha_l|\alpha_l\rangle = 1$, and $\langle\alpha_l|\beta_k\rangle = 0$ for $\alpha \neq \beta$ and $l \neq k$. Moreover, in a general quantum basis set $\{|j\rangle\}$, obtained for the time-independent portion of the Hamiltonian, $\mathcal{H}_0$, one can always expand the Floquet sidebands as a superposition $|\alpha_l\rangle = \sum_j f_{\alpha lj}|j\rangle$ (with $\sum_{lj}|f_{\alpha lj}|^2 = 1$), and hence expand the Floquet modes in terms of the time-independent basis. Inserting Eq. (S6) in Eq. (S5) yields a quasienergy eigenvalue equation, similar to the time-independent Schrödinger equation, in an extended (spatial and temporal) Hilbert space (or Sambe space) [11]. By solving this eigenvalue problem, one finds quasienergies and Floquet sidebands and, accordingly, can construct the Floquet modes and states [9, 12, 13].

The secular matrix of this system of eigenvalue equations is real and symmetric, so it possesses $N_{\rm F}$ (truncation number of the eigenvalue problem) real eigenvalues ε_α, with N_j of them confined within a ω_M range of energy scale,

and their corresponding real eigenvectors $|\alpha_l\rangle$. In addition, $\varepsilon_{\alpha n} \equiv \varepsilon_\alpha + n\omega_M$ (note that we can set $\varepsilon_\alpha = \varepsilon_{\alpha 0}$ for the first BZ) and $|\alpha_{l+n}\rangle$ are also eigenvalues and eigenvectors for any integer n. This means that the following transformations $\varepsilon'_\alpha = \varepsilon_\alpha + n\omega_M$ and $|\alpha'(t)\rangle = \mathrm{e}^{\mathrm{i}n\omega_M t}|\alpha(t)\rangle$, convert any eigenstate of the Floquet Hamiltonian into another eigenstate. This yields an identical solution to that in $|\psi_\alpha(t)\rangle$, but with the shifted quasienergy $\varepsilon_\alpha \to \varepsilon_{\alpha n} \equiv \varepsilon_\alpha + n\omega_M$. This repetition (periodicity in the quasienergies) constructs Brillouin zones (BZs) of length ω_M for each l in the energy scale of the system. Consequently, the distinction between the ground and the excited states is expressed before the mechanical oscillation is turned on where there is no Floquet system, yet. After the vibration is turned on and the system is in the Floquet picture, there is no distinction between the quasienergy states. The nomenclature based on the parameter α used here is then related to the nomenclature prior to the vibration and their order in the primary BZ to be able to refer to them precisely, but does not mean/imply the order of the states and/or a distinction between the ground or excited states [14, 15].

In the Fourier expansion of the time-dependent Hamiltonian, it is expected to collect a sufficient number of terms to project on the desired higher-order processes. Namely, $m_{\max}$ describes, mathematically, the maximum order of the Hamiltonian terms in the Fourier expansion ($|m| \leq m_{\max}$), and, physically, implies the number of particles (mechanical oscillation quanta) that the source can provide to exchange with the system through the first-order process. On the other hand, $l_{\max}$ is the maximum number of quanta that the subsystems can potentially exchange through the process, in all different orders, so that potentially it is expected to meet $m_{\max} \leq l_{\max}$. Here, it is also expected to choose $m_{\max} \geq N_j$ and $l_{\max} \geq N_j$, so that the drive and the internal interaction provide enough external quanta for the system to at least be able to make the transition between the ground state and the highest potentially possible truncated excited state if necessary. In the present work, we calculate ε_α and $|\alpha(t)\rangle$ typically for the QRM with N_j dressed levels by retaining only $|l| \leq l_{\max}$ [therefore, $N_{\mathrm{F}} = N_j(2l_{\max}+1)$] terms and numerically solving the resulting finite system of equations until convergence within this section. After normalization, these solutions must satisfy the orthogonality and completeness criteria, and also [10] $\sum_\alpha \varepsilon_\alpha = \sum_j E_j$, modulus ω_M.

A. Floquet master equation approach to calculate the expectation value of an operator

Observables can also be computed from the master equation density matrix (with a finite basis). Knowing that the Floquet states construct a complete basis, it is desirable to expand the density matrix in the Floquet representation as $\rho(t) = \sum_{\alpha\beta} \rho_{\alpha\beta}(t)\, |\alpha(t)\rangle\langle\beta(t)|$, where $\rho_{\alpha\beta}(t) \equiv \langle\alpha(t)|\rho(t)|\beta(t)\rangle$. This allows us to write the von-Neumann equation for the system density matrix as [16]

$$\partial_t \rho_{\alpha\beta}(t) = -\mathrm{i}(\varepsilon_\alpha - \varepsilon_\beta)\rho_{\alpha\beta}(t), \tag{S7}$$

for a closed system without any dissipation, where it yields the analytical solution,

$$\rho_{\alpha\beta}(t) = \rho_{\alpha\beta}(0)\, \exp\{-\mathrm{i}(\varepsilon_\alpha - \varepsilon_\beta)t\}, \tag{S8}$$

up to a given initial condition. In order to configure this initial condition into the above solution, one should express the initial condition in the Floquet modes basis. To do so, we obtain the Floquet matrix elements of both sides to give $\rho_{\alpha\beta}(0) = \langle\alpha|j=0\rangle\langle j=0|\beta\rangle$. Having obtained the time evolution of the density matrix, we can calculate the average value of observables throughout the time progression. In the Schrödinger picture, for any arbitrary operator O, we have: $\langle O(t)\rangle = \mathrm{tr}\,\{O\rho(t)\}$. We note that the periodicity of an averaging quantity concerning an observable can be attained by the same technique of adding dissipation as mentioned in the main text.

One can find the density matrix and then calculate the expectation value in the time-independent basis of the renormalized DC Hamiltonian. However, knowing that the change of basis does not change the trace, we can find a simpler and more computationally efficient formula using the Floquet basis via

$$\begin{aligned}\langle O(t)\rangle &= \sum_{\alpha\beta} O_{\alpha\beta}(t)\rho_{\beta\alpha}(t) \\ &= \sum_{\alpha\beta l} O_{\alpha\beta l}\rho_{\beta\alpha}(0)\, \mathrm{e}^{\mathrm{i}(\varepsilon_\alpha - \varepsilon_\beta + l\omega_M)t},\end{aligned} \tag{S9}$$

where $O_{\alpha\beta l} = (1/T)\int_0^T dt\, \mathrm{e}^{-\mathrm{i}l\omega_M t}\, O_{\alpha\beta}(t)$. Therefore, in the steady state, we obtain $\langle O(t)\rangle_{\mathrm{ss}} = \sum_{\alpha l} O_{\alpha\alpha l}\rho_{\alpha\alpha}(0)\, \mathrm{e}^{\mathrm{i}l\omega_M t}$,

and the average of the expectation value reads

$$\overline{O} \equiv \frac{1}{T}\int_0^T dt\,\langle O(t)\rangle_{\rm ss} = \sum_\alpha O_{\alpha\alpha 0}\rho_{\alpha\alpha}(0). \tag{S10}$$

This formula gives the same results as the formula presented in the main text, but using the extended space formalism [12, 13], in less computational time.

B. Time evolution and transition probability

To find the evolution of an arbitrary state $|\psi(t)\rangle$, we use the fact that the set of solutions to Schrödinger's equation, $|\psi_\alpha(t)\rangle$ forms a complete basis. A general time-periodic Hamiltonian satisfying the unitary time evolution generates the operator,

$$U(t,t_0) = \mathcal{T}\exp\{-{\rm i}\int_{t_0}^t dt'\,\mathcal{H}_{\rm FQR}(t')\}, \tag{S11}$$

where $\mathcal{T}$ is the Wick's time-ordering operator. The time evolution operator, expressed in Floquet quasienergy eigenstates of $\mathcal{H}_{\rm FQR}(t)$, is

$$U(t,t_0) = \sum_\alpha {\rm e}^{-{\rm i}\varepsilon_\alpha(t-t_0)}\,|\alpha(t)\rangle\langle\alpha(t_0)|. \tag{S12}$$

The transition probability from an initial quantum state of the renormalized static Hamiltonian, $|j=i\rangle$, to a final quantum state, $|j=f\rangle$, is closely related to the matrix elements of the time evolution operator $U_{fi}(t,t_0) \equiv \langle f|U(t,t_0)|i\rangle$. In Floquet theory, $U_{fi}(t,t_0)$ can be interpreted as the amplitude that the system initially in the Floquet joint state $|i\rangle$ and zero mechanical oscillation at time t_0 evolves to the Floquet joint state $|f\rangle$ and k mechanical oscillation by time t, according to the time-independent Floquet Hamiltonian $\mathcal{H}_{\rm F}$, with some weighting factors that must be summed over all final quantum processes and states [17–19]. The transition probability going from the initial quantum state and a coherent mechanical oscillation state to the final quantum state summed over all final mechanical oscillation quantum process orders reads $P_{f\leftarrow i}(t,t_0) = |U_{fi}(t,t_0)|^2$.

The quantity of practical (experimental) interest, however, is the transition probability averaged over initial times t_0 (or, equivalently averaged over the initial phases of the external drive seen by the system), keeping the elapsed time $(t-t_0)$ fixed. Moreover, averaging over $(t-t_0)$, one obtains the long-time average transition probability [17–19], $\overline{P}_{f\leftarrow i} = \sum_{l,l'}\overline{P}^{(l,l')}_{f\leftarrow i}$, with

$$\overline{P}^{(l,l')}_{f\leftarrow i} = \sum_\alpha |\langle f|\alpha_l\rangle\langle\alpha_{l'}|i\rangle|^2. \tag{S13}$$

Also, the order of the mechanical oscillation involved in the quantum process for the higher-order processes is portrayed by the number $n = l - l'$, with the associated probability of $\overline{P}^{(n)}_{f\leftarrow i} = \sum_{l-l'=n}\overline{P}^{(l,l')}_{f\leftarrow i}$, so that $\overline{P}_{f\leftarrow i} = \sum_n \overline{P}^{(n)}_{f\leftarrow i}$.

S3. ALTERNATIVE FORMS OF PERIODIC TIME MODULATION

Instead of a pure sinusoidal modulation, one may use other forms of periodic modulation to Floquet-engineer quantum systems [20]. Indeed, provided that the waveform is still periodic, we can always use Floquet theory.

We can let the general form of the normalized coupling with an arbitrary shape be $\eta(t) = \eta_0 + \eta_M(t)$, with the dynamical part having the peak value of η_M. Accordingly, the FQR model Hamiltonian becomes

$$\mathcal{H}_{\rm FQR}(t) = \omega_{\rm c}a^\dagger a + \frac{\omega_a}{2}\left\{\frac{\sigma_z - {\rm i}\sigma_y}{2}\,{\rm e}^{{\rm i}2(a+a^\dagger)\eta_0}\,{\rm e}^{{\rm i}2(a+a^\dagger)\eta_M(t)} + \frac{\sigma_z + {\rm i}\sigma_y}{2}\,{\rm e}^{-{\rm i}2(a+a^\dagger)\eta_0}\,{\rm e}^{-{\rm i}2(a+a^\dagger)\eta_M(t)}\right\}. \tag{S14}$$

Now we can expand in the Fourier series: $\mathcal{H}_{\rm FQR}(t)=\sum\mathcal{H}_m\,{\rm e}^{{\rm i}m\omega_M t}$, where $\mathcal{H}_m=(1/T)\int_0^T dt\,{\rm e}^{-{\rm i}m\omega_M t}\,\mathcal{H}_{\rm FQR}(t)$.

Popular shapes of modulation exist that can be more productive than the pure sinusoidal case (shown in the main text), since they can produce more effective nonadiabatic evolutions, such as the latching modulation and the ramp modulation [20]. A latching modulation is, in one cycle, given by

$$s(t)=\begin{cases}2d, & 0<t/T<1-d,\\ -2(1-d), & 1-d<t/T<1,\end{cases}\tag{S15}$$

where d is the duty-cycle ratio. Note that for a symmetric latching modulation, with $d=1/2$, we have $s(t)=\mathrm{sgn}\{\cos\omega_M t\}$. Then, we take $\eta_M(t)=\eta_M s(t)$, and obtain

$$\begin{aligned}\mathcal{H}_0&=\omega_{\rm c}a^\dagger a+\frac{\omega_a}{2}\left\{\frac{\sigma_z+{\rm i}\sigma_y}{2}\,{\rm e}^{-{\rm i}2(a+a^\dagger)\eta_0}+\frac{\sigma_z-{\rm i}\sigma_y}{2}\,{\rm e}^{{\rm i}2(a+a^\dagger)\eta_0}\right\}\cos[2(a+a^\dagger)\eta_M],\\ \mathcal{H}_m&=\frac{\omega_a[1-(-1)^m]}{2\pi m}\left\{\frac{\sigma_z+{\rm i}\sigma_y}{2}\,{\rm e}^{-{\rm i}2(a+a^\dagger)\eta_0}-\frac{\sigma_z-{\rm i}\sigma_y}{2}\,{\rm e}^{{\rm i}2(a+a^\dagger)\eta_0}\right\}\sin[2(a+a^\dagger)\eta_M],\quad m\neq 0.\end{aligned}\tag{S16}$$

The ramp modulation (sawtooth wave) is defined via

$$r(t)=2(t+\tau)/T,\quad -T/2\leq t<T/2,\quad r(t+T)=r(t),\tag{S17}$$

and we take $\eta_M(t)=\eta_M r(t)$. In this case,

$$\mathcal{H}_m=\omega_{\rm c}a^\dagger a\,\delta_{m0}+(-1)^m\frac{\omega_a}{2}\left\{\frac{\sigma_z-{\rm i}\sigma_y}{2}\,\frac{{\rm e}^{{\rm i}2(a+a^\dagger)(\eta_0+2\eta_M\tau/T)}}{-m\pi+2(a+a^\dagger)\eta_M}-\frac{\sigma_z+{\rm i}\sigma_y}{2}\,\frac{{\rm e}^{-{\rm i}2(a+a^\dagger)(\eta_0+2\eta_M\tau/T)}}{-m\pi-2(a+a^\dagger)\eta_M}\right\}\sin[2(a+a^\dagger)\eta_M].\tag{S18}$$

This can also be separated as

$$\begin{aligned}\mathcal{H}_0&=\omega_{\rm c}a^\dagger a+\frac{\omega_a}{2}\left\{\frac{\sigma_z-{\rm i}\sigma_y}{2}\,{\rm e}^{{\rm i}2(a+a^\dagger)(\eta_0+2\eta_M\tau/T)}+\frac{\sigma_z+{\rm i}\sigma_y}{2}\,{\rm e}^{-{\rm i}2(a+a^\dagger)(\eta_0+2\eta_M\tau/T)}\right\}\frac{\sin[(a+a^\dagger)\eta_M]}{2(a+a^\dagger)\eta_M},\\ \mathcal{H}_m&=(-1)^m\frac{\omega_a}{2}\left\{\frac{\sigma_z-{\rm i}\sigma_y}{2}\,\frac{{\rm e}^{{\rm i}2(a+a^\dagger)(\eta_0+2\eta_M\tau/T)}}{-m\pi+2(a+a^\dagger)\eta_M}-\frac{\sigma_z+{\rm i}\sigma_y}{2}\,\frac{{\rm e}^{-{\rm i}2(a+a^\dagger)(\eta_0+2\eta_M\tau/T)}}{-m\pi-2(a+a^\dagger)\eta_M}\right\}\sin[2(a+a^\dagger)\eta_M],\quad m\neq 0.\end{aligned}\tag{S19}$$

We later show a selection of results on the productivity of the sawtooth (ramp) modulation using Eq. (S19) with having $\tau=0$ fixed.

S4. ADDITIONAL NUMERICAL RESULTS AND DISCUSSIONS

In this section, we provide some additional numerical results to complement the understanding of the main paper results.

A. Ground-state virtual photons as a function of the static and dynamical coupling rates

First, we show the ground-state virtual populations of the cavity-QED system, which are unique to the USC regime. In Fig. S1(a), we plot the $\mathcal{H}_0$ ground-state virtual photons versus the static and dynamical coupling rates. Note that when $\eta_M=0$, we obtain the limit of the pure QRM, and its renormalized case occurs when $\eta_M\neq 0$. In panel (b), we fix the value of $\eta_M=0.5$ for the renormalized time-independent (TI) Hamiltonian and compare the result with the pure QRM case where $\eta_M=0$. From this panel, we see that, as expected, due to the dipole nonlinearity, the TLS excitation plots are generally lower than their cavity counterparts for larger η_0. Moreover, we see that the DC renormalization due to the mechanical oscillation lowers the occupation of the virtual excitations. Note, because the

effect of the dynamical coupling is in the USC range, it adds a nonzero value to the starting tale of the cavity virtual excitation even before when the static coupling enters the USC regime, i.e. $\eta_0 < 0.1$, while there is no contribution for that of the TLS counterpart. This is because the renormalization is due to the Bessel function with the photonic-only operator argument $2(a^\dagger + a)\eta_M$, thus it only influences the photonic portion when there is no static light-matter coupling. We note that, in the absence of the static light-matter coupling, the eigenstate of the time-independent system is the joint state of the bare light and the bare matter eigenstates, so that the photonic and the matter operators can be disjointed and separately applied to the joint bare ground states; hence, there is no new effect for the TLS ground state excitation when $\eta_0 = 0$ due to the renormalization of the QRM.

We stress that the virtual populations are not physical in the sense that they cannot be measured, and indeed their value, like the definition of entanglement, is a gauge-dependent quantity. This is in contrast to the real populations and the physical observables that are computed with a gauge-invariant theory [5].

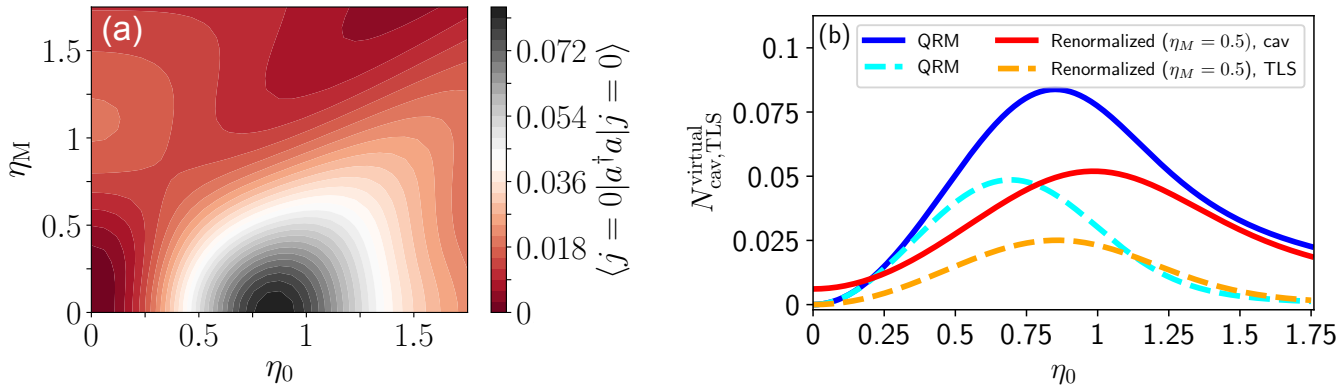

Figure S1. **Ground-state virtual excitations.** We show the population of the QR-dressed ground state excitations, also known as the virtual excitations in the ground state of the (time-independent) QRM. Panel (a) depicts a 2D plot of the virtual cavity photons, versus the static and dynamical coupling strengths. In panel (b), the variations of the cavity and TLS virtual excitations are shown when $\eta_{\mathrm{M}} = 0$ and $\eta_M = 0.5$ versus the change of the static coupling, η_0. In this panel, the solid blue line/dashed cyan line represents the populations of virtual photons/TLS excitations in the QR-dressed ground state. This population is finite because the initial-time ground state of the system is an entangled state of photonic and atomic excitations, defined from $|j=0\rangle = \sum_{k=0}^{\infty}\langle g, 2k|j=0\rangle|j=0\rangle + \langle e, 2k+1|j=0\rangle|j=0\rangle$.

To appreciate the physics of the excitation number trends, we need to gain insight into the *higher-order quantum and time-driven harmonic processes*, and the interplay among them that generate peak and valley structures (in the plots of populations versus pumping parameters and frequency). Generally, higher multi-oscillation peaks are narrower than one-oscillation peaks and they also form earlier (smaller values) in amplitude and frequency of the drive. In order to analyze the spectral structures in panels (c) and (d) of Fig. 3 of the main text, we plot the same spectra here, i.e., in Figs. S2 and S3, along with their associated eigenenergy, quasienergy, and transition probability diagrams. The structure of the excitation number spectrum is related to the transition probability between the initial (ground) state and the final state and the interplay among those transitions which are, in turn, related to each individual anticrossing, as well as the interplay between neighbouring anticrossings in the Floquet quaienergy spectra. We also note that the anticrossings in the quasienergy spectra are the outcomes of the original crossings and/or anticrossings in the eigenenergy spectra. More precisely, in the limit of zero drive, the quasienergies map to the eigenenergies $\varepsilon_{\alpha l} = E_{j=\alpha} + l\omega_M$ (considering the redundant periodicity of quasienergies in the extended space) [21]. As the external perturbation takes place, the quasienergies evolve from these initial values by the effect of not only the superposition of the other eigenenergy states at the places of anticrossings but also due to the AC-Stark shift. Nevertheless, the original eigenenergy crossings/anticrossing between two eigenenergy states which leads the anticrossing between two quasienergies states $|\alpha_l\rangle$ and $|\alpha'_{l'}\rangle$ shifted by $\Delta l = l - l'$ is a clear indicative of an existing transition mediated by Δl mechanical oscillation.

B. Variation of the Floquet engineering process versus the amplitude of the dynamical coupling parameter η_M

To help appreciate the dynamically-modified transitions, consider the QRM ground state at $t = 0^+$. As time evolves, with $\eta_M \neq 0$, the ground state adiabatically transforms into a Floquet state. At the first anticrossing between a Floquet sideband of the lower state and a Floquet sideband of a higher state, where a superposition of the Floquet sidebands is constructed, a diabatic transition occurs, $|\alpha_l\rangle \rightarrow |\alpha'_{l'}\rangle$ at the anticrossing where a superposition $a|\alpha_l\rangle + a'|\alpha'_{l'}\rangle$ is provided. Then, the created superposition, generally oscillating at a multiple of the stimulation frequency $\Delta\varepsilon = n\omega_M$, adiabatically transforms into the superposition of the two original QRM states, and now oscillates at their energy difference, $E_{kj} = E_k - E_j$. Depending on the size of ω_M, one can go back and forth among different BZs to form a transition between the QRM states, if it is parity allowed.

In Fig. S2, we plot the variation of the Floquet engineering process versus the amplitude of the dynamical coupling parameter η_M, where we show: (a) the eigenenergies (shifted) in the extended space, (b) quasienergies in a BZ, (c) transition probabilities for the major contributions, and (d) the exciation number spectra. We highlight that the major cavity double-peak and valley structure in Fig. S2(d) is actually formed by the combination of a 3-ω_M resonance transition (from $|j = 0\rangle \rightarrow |j = 3\rangle$) and a 15-$\omega_M$ resonance transition (from $|j = 0\rangle \rightarrow |j = 15\rangle$). These peaks are associated with the major green and red peaks in the corresponding transition probability plot in panel (c), respectively, and the most effective associated anticrossing (shown by green and red circles) in panel (b). Remarkably, the red-circle anticrossing is originally created due to the anticrossings of the ground eigenstate (solid blue) and the fifteenth eigenstate (dashed red), altogether shifted by $15\omega_M$, as shown in panel (a); this also has a gradual AC-Stark shift, as seen in panel (b), and is power broadened as the number of oscillating harmonics increases, as shown in panels (c,d). Thus, in the first BZ, as depicted in Figs. S2(b), we observe the most effective corresponding anticrossing at the same point (red circle) between the two Floquet sidebands $|\alpha_l = 12_l\rangle$ (indigo-colored line) and $|\alpha_l = 14_l\rangle$ (dark orange-colored line). Here, we name the Floquet mode $\alpha \equiv j$ based on the fact that at the limit of $\eta_M \rightarrow 0^+$ they reach their corresponding number j (renormalized DC states). The former sideband is connected adiabatically to $|j = 15\rangle$ via $|\alpha'_{l'} = 12_{l+14}\rangle$, and the latter sideband translates to $|\alpha'_{l'} = 14_{l-1}\rangle$, to adiabatically construct the $|j = 0\rangle$ renormalized-QRM state. Hence, the transition is a 15-ω_M event.

Similarly, by investigation and comparison of the plots in Figs. S2, one can conclude that the other major peak at $\eta_M \approx 0.56$ in Fig. S2(d) corresponds to the transition probability [left dashed red peak in panel (c)] and the anticrossing shown by the left red circle in panel (b) between the two Floquet sidebands $|\alpha_l = 12_l\rangle$ and $|\alpha_l = 4_l\rangle$. This anticrossing is due to the crossing of the dashed red line representing $E_{15} - 14\omega_M$ (or, more generally, $E_{15} - l'\omega_M$) and the solid blue line representing $E_0 + \omega_M$ (or, more generally, $E_0 + l\omega_M$) in panel (a) which is modified through the AC-Stark shift. According to the transition probability plot in panel (b), this is then a 15-ω_M peak ($n \equiv \Delta l = l' - l = -15$, meaning that fifteen energy packets of mechanical oscillation are absorbed from the external mechanical drive) that is coming from the transition between the ground state and the fifteenth excited state of the renormalized-QRM DC Hamiltonian. The former sideband is again connected adiabatically to $|j = 0\rangle$ via $|\alpha'_{l'} = 12_{l-1}\rangle$ sideband, and the latter sideband translates to $|\alpha'_{l'} = 4_{l+14}\rangle$ to adiabatically construct the $|j = 15\rangle$ renormalized-QRM state. Hence, the transition is a 15-ω_M quantum process.

Similar explanations can be used for the remaining peaks or the spectral variations. However, further investigation on Fig. S2 shows evidence of additional nonlinear effects. For example, by comparing the peaks versus η_M we observe the power broadening of the peaks as η_M increases due to the nonlinear addition of the higher-order process as well as the dynamical AC-Stark shifts. Moreover, the constructive/destructive interplay among the higher-order peaks is quite remarkable, which can lead to various light-matter phenomena, such as the creation of Fano resonances, electromagnetically induced transparency, and Autler-Townes (multiplet) splitting effect [see, e.g., the interplay between the dashed red and black lines in Fig. S2(c)], particularly in the TLS number spectra [17, 22, 23].

C. Spectral features versus the external mechanical oscillation frequency

In Fig. S3, we analyze the spectral features versus the external mechanical oscillation frequency (ω_M, in units of ω_c) for fixed values of $\eta_0 = 0$, $\eta_M = 0.5$ and $\omega_a = \omega_c$. Here, again because the switching on/off is already in the USC regime, $\eta_M > 0.1$, with the nonzero input energy one expects to gradually see the production of real excitation numbers. Further, besides the resonant multi-mechanical oscillation peaks, the production of real excitations generally

increases, as the input energy increases, unless there is a competing nonlinear effect or destructive superposition of peaks. The multi-oscillation res onance peaks can be connected to the quasienergy spectrum as before. Moreover, we know that the time-independent eigenenergy spectra must be constant in ω_M because they are independent of the dynamical coupling frequency. More precisely, the QRM eigenenergies are independent of both amplitude and frequency of the dynamical coupling, but only depend on the static coupling; whereas the renormalized time-independent Hamiltonian is independent of the drive frequency but depends on the amplitude of the dynamical and static couplings. Also, because the dynamical coupling is nonzero, $\eta_M = 0.5$, we expect a discrepancy between the QRM and the renormalized eigenenergies due to the modification of the DC component (similar effect as also seen in Fig. S1).

In Fig. S3(a), we note that because initially $\varepsilon_\alpha = E_{j=\alpha}$ is constant versus ω_M, the lines with slope l of $\varepsilon_{\alpha l} = E_{j=\alpha} + l\omega_M$ pass through the point $\varepsilon_\alpha = E_{j=\alpha}$ in the vertical axis. Evidently, one can see a pattern of the AC-Stark shifted lines resembling those lines in the quasienergy spectrum in panel (b); for example, this is shown with the lower and upper thick blue lines of E_0 and $E_0 + \omega_M$, respectively, and the pattern of straight lines (with mix indigo and darkorange colors) closely following it (showing AC-Stark shifting). All these patterns of straight lines in the quasienergy versus ω_M diagram resemble eigenenergy lines of the renormalized DC Hamiltonian shifted among different BZs with their own specific AC-Stark shifts. A similar analysis of the previous figure can be applied here to understand the spectrum structure and creation of peaks and dips. For example, one observes a major peak at $\omega_M \approx 0.6\omega_c$ in Fig. S3(d) which is mainly due to the (9-ω_M) transition between the ground and the tenth excited stated of the renormalized DC Hamiltonian as shown in panel (c) and the corresponding anticrossing in the quasienergy diagram of panel (b) shown by the same color circle. Notably, we see in panel (a) that this anticrossing is originally created due to the crossing of the solid blue and dashed black lines undergone through AC-Stark shift. We see a complete description of other major peaks and transitions in Fig. S3.

D. Quasienergy and number spectra versus the static coupling

In Fig. S4, we show the variation of the quasienergy and number spectra versus the static coupling for fixed values of $\eta_M = 0.5$, $\omega_a = \omega_c$ and $\omega_M = 0.5\omega_c$. We again see the multi-oscillation resonance peaks. An important characteristic of the plots in panel (d) of this figure is their nonzero values at $\eta_0 = 0$. This is because we chose $\eta_M = 0.5$, which means that the switching on/off event is already in the USC regime even with the zero static coupling, so that the production of real excitations occurs even if $\eta_0 = 0$. The analysis of the peaks is similar to those of the previous two figures and a description of the peaks is given in the figure.

In panels (a-d) of Fig. S5, we show the evolution of real excitations versus time, for a fixed value of η_0 and nonzero dynamical coupling, $\eta_M = 0.2$ (a,b) and $\eta_M = 0.5$ (c,d). We observe in panels (a) and (c), which is for a closed system with no dissipation, the excitation numbers are not quite periodic, but when the dissipation (and/or prethermalization) is introduced in panels (b) and (d), the graphs are pure periodic with the same period of the mechanical oscillation drive, $T = 2\pi/\omega_M$, after a sufficiently large time, $t > t_{\rm ss}$ (we safely see that $t_{\rm ss} \sim 5T$) where they settle to a steady-state. Regardless of the dissipation, we see the discrepancy between the solid curves (real photons) and the dashed curves (TLS excitation) as the dynamical coupling increases. This is because the real transitions are between the dressed states with a mixed number of excitations, and hence the production of the real excitations is a nonlinear quantum process.

E. Sawtooth (ramp-modulated) drive converts more photons from virtual to real

Finally, we also investigate the situation of potentially more-effective waveforms for the dynamical coupling, i.e., to produce larger real excitations. As a popular example, we present the results for the dynamical coupling with a sawtooth waveform [20]. We expect that because this waveform already switches on and off nonadiabatically, *its effect in the production of real excitations must be stronger than the pure oscillatory case*, as we indeed generally see in all panels of Fig. S6 compared to the previous plots. In panels (a-d) of Fig. S6, we see the time evolution of the real excitation number where we see the periodicity of the graphs after a sufficiently large time when there is dissipation. Comparing these panels with the same panels in Fig. S5, we see that the plots are notably with larger amplitudes as well as are highly more nonlinear. We observe the discrepancy between the dashed and solid curves even with smaller

values of the dynamical coupling.

The lower panels of Fig. S6 show the average number of excitations with a sawtooth mechanical oscillation versus the variation of the static coupling for fixed values of $\eta_M = 0.5$ and $\omega_M = 0.5\omega_c$ (e), the variation of the dynamical coupling for fixed values of $\eta_0 = 0$ and $\omega_M = 0.5\omega_c$ (f), and the variation of the mechanical oscillation frequency for fixed values of $\eta_0 = 0$ and $\eta_M = 0.5$ (g), all for $\omega_a = \omega_c$. Again, we see a comparatively higher amplitude in all of these plots *due to the effectiveness of the sawtooth excitation* as compared to pure sinusoidal excitation.

We also see multi-oscillation peaks in the spectra as expected due to the nonperturbative process of excitation. Strikingly, we see in panel (g) that when the frequency is quite small, there is a negligible amount of real excitation production because it takes a large time for the system to see a nonadiabatic change. However, we see numerous multi-oscillation peaks as the frequency is large enough as well as the stronger discrepancy between the cavity and TLS excitations. These three stronger characteristics in the sawtooth waveform plots compared to those of the sinusoidal plots, i.e, the larger amplitudes of graphs, the larger discrepancy between the cavity and TLS graphs, as well as the larger and stronger multi-oscillation peaks in the graphs, imply the high effectiveness of a more nonadiabatic waveform in the generation of high-order nonlinear quantum processes.

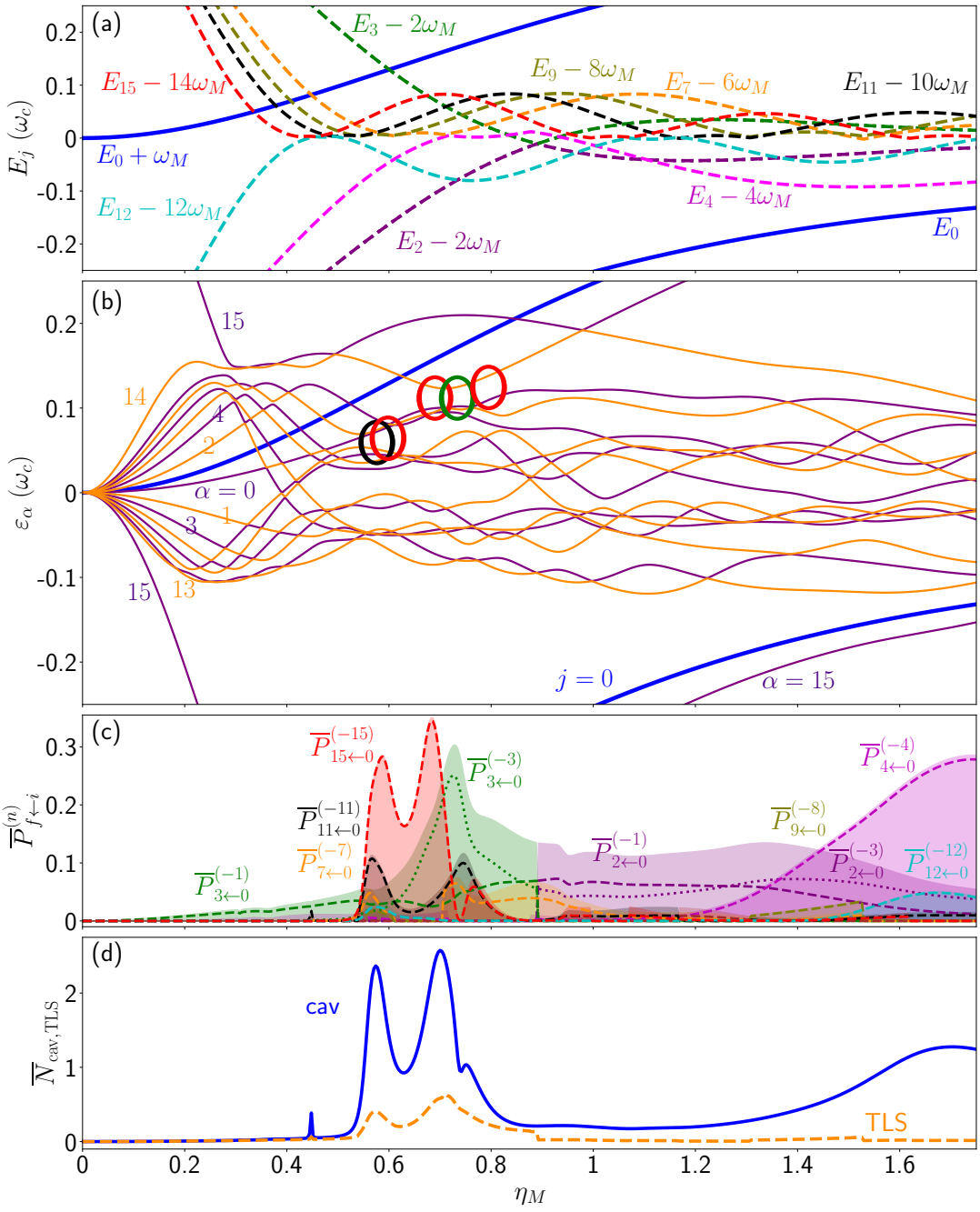

Figure S2. **Eigenenergies, transition probabilities and populations as a function of dynamical coupling strength η_M.** (a) Original crossing/anticrossings of eigenenergies of the renormalized QRM shifted into the first BZ that show the quasienergy states in the limit of zero time-dependent perturbation; they resemble the eigenstates and their shifts by multiples of the drive frequency, i.e., $\varepsilon_{\alpha l} \equiv E_{j=\alpha} + l\omega_M$ is the zeroth order perturbation of the Floquet quasienergies. (b) Floquet quasienergy spectra for the QRM with truncation number of states $N_j = 16$ in the first BZ. The lower thick blue line is the ground eigenstate energy line E_0 and the upper thick blue line shows its shift by a single drive frequency, $E_0 + \omega_M$, to represent it in the first BZ. The bi-colored (indigo and dark orange) patterned lines closely following these two blue lines show gradual evolution of the quasienergy states of the ground energy state undergone through AC-Stark shift. The color-coded lines in this panel represent different Floquet quasienergies (for better visualization of the anticrossings), and the circles show the anticrossings corresponding to some of the major transitions with the same color in panel (c). (c) Major transitions' probabilities $\overline{P}^{(n)}_{f\leftarrow i}$ (constructing the total transition probability $\overline{P}_{f\leftarrow i}$, shown by the corresponding same-color shaded area), and (d) real excitation number spectrum for the cavity (solid) and the TLS (dashed), versus the dynamical coupling amplitude η_M. The graphs are obtained for $\eta_0 = 0$, $\omega_a = \omega_c$, $\omega_M = 0.5\omega_c$, $m_{\max} = l_{\max} = 20$.

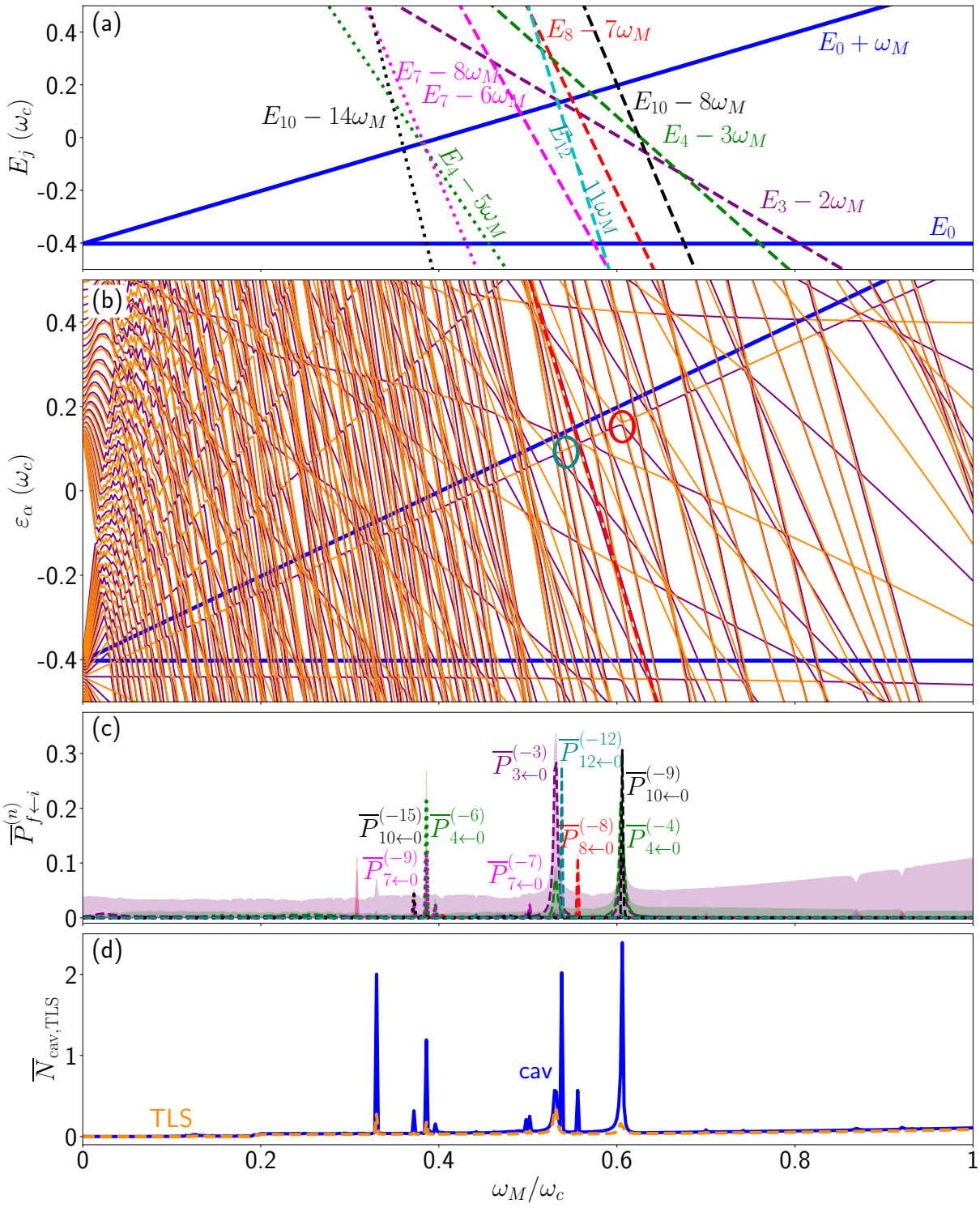

Figure S3. **Eigenenergies, transition probabilities and populations as a function of mechanical drive frequency ω_M.** As in Fig. S2, but with fixed values of $\eta_0 = 0$, $\eta_M = 0.5$ and $\omega_a = \omega_c$.

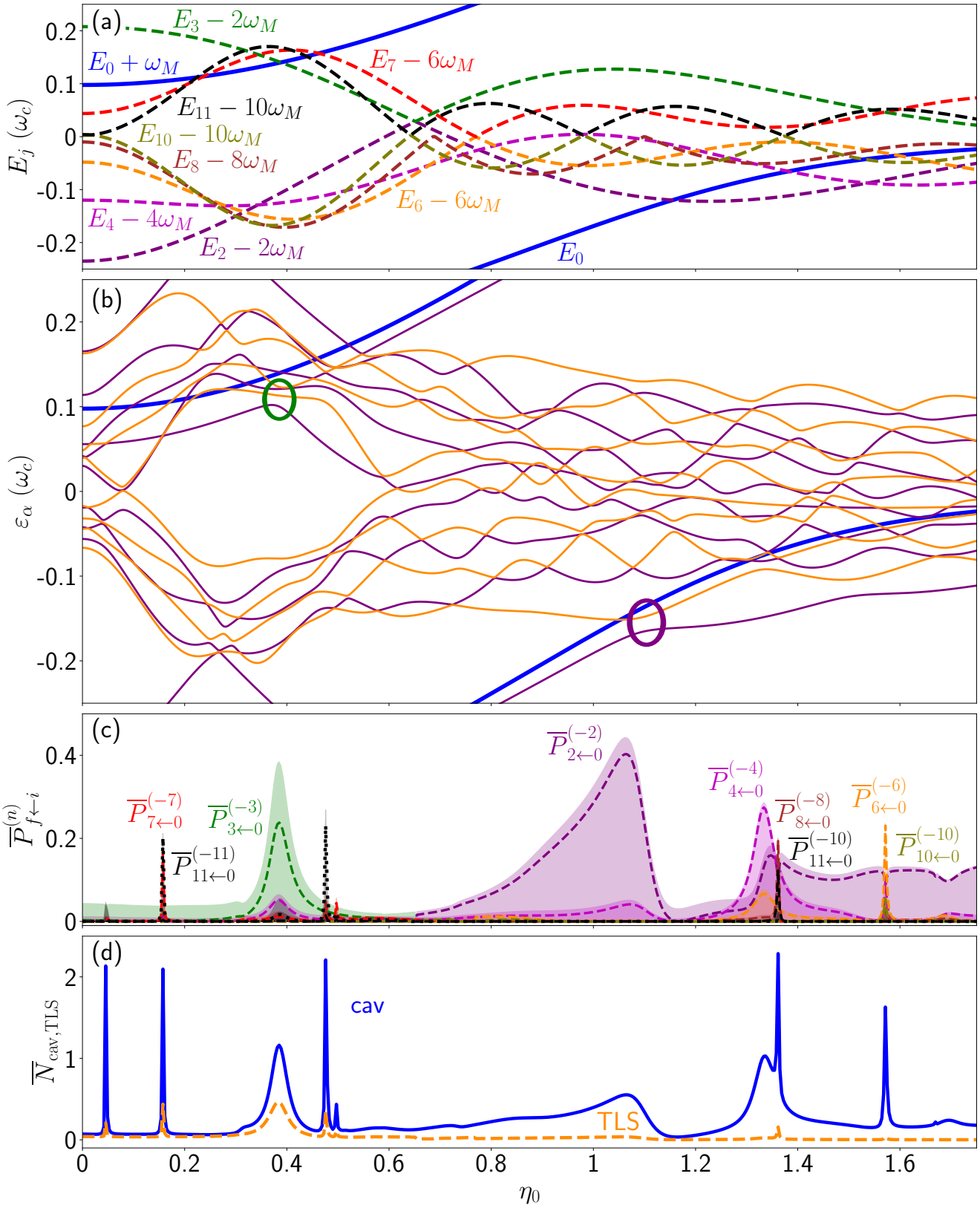

Figure S4. **Eigenenergies, transition probabilities and populations as a function of static coupling strength η_0.** As in Fig. S2, but with fixed values of $\eta_M = 0.5$ and $\omega_M = 0.5\omega_c$ and $\omega_a = \omega_c$.

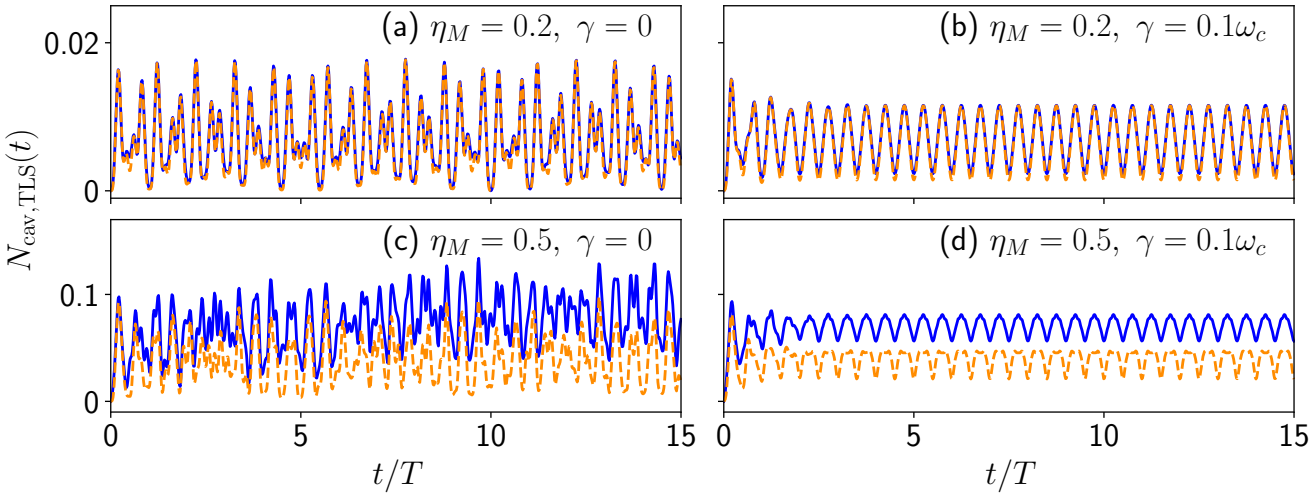

Figure S5. **Time-dependent real excitation numbers for different η_M.** An example of the time-dependent real excitations, $N_{\mathrm{cav}}(t)$ (real photons, solid blue line) and $N_{\mathrm{TLS}}(t)$ (real TLS excitation, dashed orange line) are shown for (a,b) $\eta_{\mathrm{M}} = 0.2$, and (c,d) $\eta_{\mathrm{M}} = 0.5$, with $\eta_0 = 0$. For (a,c) there is no dissipation introduced but for (b,d) $\gamma = 0.1\omega_M$. The graphs are obtained for $m_{\max} = l_{\max} = 20$, and $\omega_a = \omega_c$, and $\omega_M = 0.5\omega_c$.

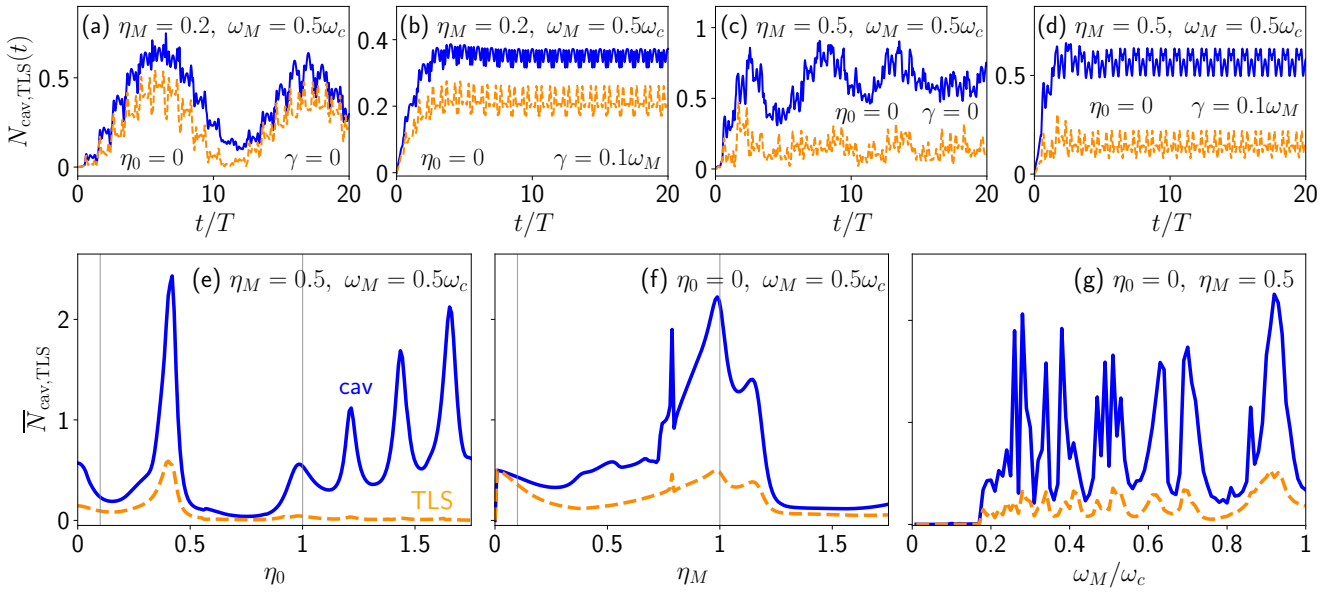

Figure S6. **Sawtooth modulation waveform.** An example of the time-dependent real excitations, $N_{\mathrm{cav}}(t)$ (real photons, solid blue line) and $N_{\mathrm{TLS}}(t)$ (real TLS excitation, dashed orange line) are shown for (a,b) $\eta_{\mathrm{M}} = 0.2$, and (c,d) $\eta_{\mathrm{M}} = 0.5$, with $\eta_0 = 0$. For (a,c) there is no dissipation introduced but for (b,d) $\gamma = 0.1\omega_M$. Panels (e,f,g) depict the *mean excitation number* that is the temporal average of the cavity excitation number, $\overline{N}_{\mathrm{cav}}$ (solid blue line) and the TLS excitation number, $\overline{N}_{\mathrm{TLS}}$ (dashed orange line). The graphs are obtained for $\eta_0 = 0$, $\omega_a = \omega_c = 2\omega_M$ (a,b,c,d), and $\tau = 0$, $N_j = 15$, $m_{\max} = l_{\max} = 20$.

REFERENCES

[1] D. De Bernardis, P. Pilar, T. Jaako, S. De Liberato, and P. Rabl, Breakdown of gauge invariance in ultrastrong-coupling cavity QED, Phys. Rev. A **98**, 053819 (2018).

[2] O. Di Stefano, A. Settineri, V. Macrì, L. Garziano, R. Stassi, S. Savasta, and F. Nori, Resolution of gauge ambiguities in ultrastrong-coupling cavity quantum electrodynamics, Nat. Phys. **15**, 803 (2019).

[3] D. Braak, Integrability of the Rabi model, Phys. Rev. Lett. **107**, 100401 (2011).

[4] C. Gustin, S. Franke, and S. Hughes, Gauge-invariant theory of truncated quantum light-matter interactions in arbitrary media, Phys. Rev. A **107**, 013722 (2023).

[5] A. Settineri, O. Di Stefano, D. Zueco, S. Hughes, S. Savasta, and F. Nori, Gauge freedom, quantum measurements, and time-dependent interactions in cavity QED, Phys. Rev. Res. **3**, 023079 (2021).

[6] W. Salmon, C. Gustin, A. Settineri, O. D. Stefano, D. Zueco, S. Savasta, F. Nori, and S. Hughes, Gauge-independent emission spectra and quantum correlations in the ultrastrong coupling regime of open system cavity-QED, Nanophotonics **11**, 1573 (2022).

[7] A. I. Nikishov and V. I. Ritus, Quantum Processes in the Field of a Plane Electromagnetic Wave and in a Constant Field 1, Sov. Phys. JETP **19**, 529 (1964).

[8] A. Eckardt, Colloquium: Atomic quantum gases in periodically driven optical lattices, Rev. Mod. Phys. **89**, 011004 (2017).

[9] A. Eckardt and E. Anisimovas, High-frequency approximation for periodically driven quantum systems from a Floquet-space perspective, New Journal of Physics **17**, 093039 (2015).

[10] J. H. Shirley, Solution of the Schrödinger equation with a Hamiltonian periodic in time, Phys. Rev. **138**, B979 (1965).

[11] H. Sambe, Steady states and quasienergies of a quantum-mechanical system in an oscillating field, Phys. Rev. A **7**, 2203 (1973).

[12] S. Restrepo, J. Cerrillo, P. Strasberg, and G. Schaller, From quantum heat engines to laser cooling: Floquet theory beyond the Born–Markov approximation, New Journal of Physics **20**, 053063 (2018).

[13] S. Restrepo, *Driven Open Quantum Systems: Aspects of Non-Markovianity and Strong Coupling*, Ph.D. thesis, Technische Universität Berlin (2019).

[14] M. D. Schroer, M. H. Kolodrubetz, W. F. Kindel, M. Sandberg, J. Gao, M. R. Vissers, D. P. Pappas, A. Polkovnikov, and K. W. Lehnert, Measuring a topological transition in an artificial spin-1/2 system, Phys. Rev. Lett. **113**, 050402 (2014).

[15] G. Platero and R. Aguado, Photon-assisted transport in semiconductor nanostructures, Physics Reports **395**, 1 (2004).

[16] J. Hausinger, *Dissipative dynamics of a qubit-oscillator system in the ultrastrong coupling and driving regimes*, Ph.D. thesis, Universität Regensburg (2010).

[17] S.-I. Chu and D. A. Telnov, Beyond the Floquet theorem: generalized Floquet formalisms and quasienergy methods for atomic and molecular multiphoton processes in intense laser fields, Physics Reports **390**, 1 (2004).

[18] S.-K. Son, S. Han, and S.-I. Chu, Floquet formulation for the investigation of multiphoton quantum interference in a superconducting qubit driven by a strong ac field, Phys. Rev. A **79**, 032301 (2009).

[19] A. M. Satanin, M. V. Denisenko, S. Ashhab, and F. Nori, Amplitude spectroscopy of two coupled qubits, Phys. Rev. B **85**, 184524 (2012).

[20] K. Ono, S. N. Shevchenko, T. Mori, S. Moriyama, and F. Nori, Quantum interferometry with a g-factor-tunable spin qubit, Phys. Rev. Lett. **122**, 207703 (2019).

[21] M. Grifoni and P. Hänggi, Driven quantum tunneling, Physics Reports **304**, 229 (1998).

[22] S. Chu, J. V. Tietz, and K. K. Datta, Quantum dynamics of molecular multiphoton excitation in intense laser and static electric fields: Floquet theory, quasienergy spectra, and application to the HF molecule, The Journal of Chemical Physics **77**, 2968 (1982).

[23] B. Peng, S. K. Özdemir, W. Chen, F. Nori, and L. Yang, What is and what is not electromagnetically induced transparency in whispering-gallery microcavities, Nature Communications **5**, 5082 (2014).